



Minerva Access is the Institutional Repository of The University of Melbourne

Author/s:

Meng, J;Weston, L;Balendhran, S;Wen, D;Cadusch, JJ;Rajasekharan Unnithan, R;Crozier, KB

Title:

Compact Chemical Identifier Based on Plasmonic Metasurface Integrated with Microbolometer Array

Date:

2022-04-01

Citation:

Meng, J., Weston, L., Balendhran, S., Wen, D., Cadusch, J. J., Rajasekharan Unnithan, R. & Crozier, K. B. (2022). Compact Chemical Identifier Based on Plasmonic Metasurface Integrated with Microbolometer Array. *Laser and Photonics Reviews*, 16 (4), <https://doi.org/10.1002/lpor.202100436>.

Persistent Link:

<https://hdl.handle.net/11343/332233>

Compact chemical identifier based on plasmonic metasurface integrated with microbolometer array

Jiajun Meng, Luke Weston, Sivacarendran Balendhran, Dandan Wen, Jasper J. Cadusch, Ranjith Rajasekharan Unnithan, and Kenneth B. Crozier**

J. Meng, L. Weston, Dr. D. Wen, Dr. J. J. Cadusch, Dr. R. R. Unnithan, Prof. K. B. Crozier

Department of Electrical and Electronic Engineering,

The University of Melbourne, Victoria 3010, Australia

E-mail: jjajunm@student.unimelb.edu.au, kenneth.crozier@unimelb.edu.au

Dr. S. Balendhran, Prof. K. B. Crozier

School of Physics, The University of Melbourne, Victoria 3010, Australia

Dr. D. Wen

Shaanxi Key Laboratory of Optical Information Technology, School of Physical Science and Technology, Northwestern Polytechnical University, Xi'an 710129, China

Prof. K. B. Crozier

Australian Research Council (ARC) Centre of Excellence for Transformative Meta-Optical Systems, The University of Melbourne, Victoria 3010, Australia

Keywords: Chemical Sensor, Plasmonics, Infrared Spectroscopy, Microspectrometers, Machine Learning Classification

This is the author manuscript accepted for publication and has undergone full peer review but has not been through the copyediting, typesetting, pagination and proofreading process, which may lead to differences between this version and the [Version of Record](#). Please cite this article as [doi: 10.1002/lpor.202100436](https://doi.org/10.1002/lpor.202100436).

This article is protected by copyright. All rights reserved.

The identification of chemicals from their mid-infrared spectra has applications that include industrial production of chemicals, food production, pharmaceutical manufacturing, and environmental monitoring. This is generally done using laboratory benchtop tools such as the Fourier transform infrared spectrometer. Although such systems offer high performance, alternative platforms offering reduced size, weight and cost could enable a host of new applications, e.g. in consumer personal electronics. Here we experimentally demonstrate a compact microspectrometer platform for chemical identification, comprising a mid-infrared metasurface integrated with a lightweight (~ 1 g) and very small (~ 1 cm³) microbolometer-based thermal camera. We train a machine learning algorithm to analyze the microspectrometer output and classify chemicals based on their mid-infrared fingerprints. We demonstrate high accuracy identification of four liquid chemicals, concentration quantification of ethyl lactate in cyclohexane down to subpercentage levels, and the classification of food and drug samples.

1. Introduction

The traditional tool for analyzing materials via their mid-infrared (MIR) fingerprints is the Fourier transform infrared (FTIR) spectrometer. This platform has wide-ranging applications, including food and drug analysis, forensics, and environmental protection. FTIR systems offer high resolution and reliability and are thus suitable for many applications. Nonetheless, at the time of writing, there is a trend toward the miniaturization of optical systems, driven by opportunities enabled by their incorporation into consumer personal electronic devices and other platforms. This motivates the development of ultra-compact MIR spectrometers that are much smaller, lighter, lower in cost and lower in power consumption than conventional FTIR systems. Previous works on visible to near-infrared microspectrometers have employed strategies that include the miniaturization of conventional dispersive optics^[1-3], and the combination of narrowband spectral filters with complementary metal oxide semiconductor (CMOS) photodetectors^[4-7]. In recent years, considerable effort has also been placed on what are known as reconstructive spectrometer systems, which employ computational methods for the estimation of spectra. This approach has been implemented in a variety of platforms, using different approaches to engineer the spectral response of filters and/or detectors. These include

This article is protected by copyright. All rights reserved.

colloidal quantum dot spectral filters^[8], metasurfaces^[9], photonic crystals filters^[10] and nanostructured silicon photodetectors^[11-13]. Another strategy for reconstructive microspectrometers is complex spectral-to-spatial mapping^[14], which can be implemented by multimode fiber speckle patterns^[15] and in disordered photonic chips^[16]. Previous studies have also explored the miniaturization of microspectrometers for the near to mid-infrared wavelength range using micro-electromechanical systems (MEMS) technologies. These include voltage-tunable Fabry-Pérot (FP) filters^[17, 18], compact Michelson interferometers^[19], and tunable plasmonic metamaterials^[20]. These methods have been proven to be effective, but the use of MEMS technologies also requires sophisticated fabrication processes. MIR spectrometers based on silicon photonics have included those employing Mach-Zehnder interferometers^[21], and other approaches such as arrayed waveguide gratings.^[22] While impressive results have been obtained, these works also often require advanced fabrication methods and/or complicated experiment set-ups.

Many previous works can be categorized as filter array-detector array (FADA) microspectrometers^[7, 8, 10, 23-30], in which a filter array is placed on top of a detector array as the wavelength selective element. The FADA approach to MIR spectrometers has several advantages, including potentially simple fabrication processes for the filter array, the absence of a requirement for control circuits and actuators, the mechanical robustness of the system due to the lack of moving parts, and the possibility of the entire system being realized in a single chip via integration of the filters with commercially available cost-effective thermal imaging sensors. Previous studies on MIR spectrometers based on the FADA configuration have investigated linear variable filters^[29, 30] and plasmonic MIR filters^[24-26]. Plasmonic MIR filters have several advantages, including the fact that the fabrication process is relatively simple (i.e. lithography, metal evaporation and lift-off) and the fact that filter functions are defined by lithography and thus can be chosen a flexible manner. We note that Refs [24-26] reported

This article is protected by copyright. All rights reserved.

plasmonic MIR filters for MIR microspectrometers, but did not demonstrate the integration with a detector array, instead testing their approach with an FTIR microscope. Therefore, to the best of our knowledge, fully-contained MIR spectrometers based on plasmonic filters have not been experimentally demonstrated. We also note that previous works on FADA-type MIR spectrometers (Refs [24-26,29,30]) had the goal of determining the spectrum of the input light. The subsequent step of interpreting the spectrum, i.e. to identify and/or quantify the chemical species present, was not considered. While this could be performed by comparing the spectrum with the known spectra of the target chemicals, this approach is not necessarily optimal in terms of chemical identification/quantification accuracy and the time needed before an answer is obtained. This motivates the development of alternative approaches for MIR microspectrometers that skip the intermediate step of spectral reconstruction, and instead identify and/or quantify the chemical species directly from the device output, i.e. the signals from the detector array. This approach has conceptual similarities to chemical sensing using electronic noses, such as carbon nanotube chemi-resistive sensor arrays^[31], graphene field effect transistors^[32], and MXene virtual sensor arrays^[33]. It has been shown that the combination of these technologies with machine learning (ML) can be favorable, e.g. for food classification^[31, 34, 35].

In this work, we experimentally demonstrate chemical sensing and quantification using an MIR microspectrometer consisting of an infrared plasmonic metasurface integrated with a thermal imaging camera in conjunction with an ML algorithm. To the best of our knowledge, our work represents the first experimental demonstration of an integrated MIR spectrometer that uses metasurfaces. It furthermore represents the first experimental demonstration of the use of ML for chemical identification/quantification using an MIR microspectrometer. Our microspectrometer is very compact, being based on a thermal camera (FLIR Lepton 2.5) that weighs ~1 g and has a volume of

This article is protected by copyright. All rights reserved.

$\sim 1 \text{ cm}^3$,^[36]. Our plasmonic metasurface consists of gold nanostructures on an undoped silicon substrate, comprising bandpass and bandstop filters that cover the spectral range of the thermal camera's spectral response (6 to 14 μm). We note that our approach is not limited to this wavelength range, however. As our plasmonic filters are fabricated by lithography, evaporation and lift-off, their operating wavelength can be readily shifted from the visible to the mid-IR^[24, 37-46] by adjusting the geometric parameters and, if necessary, the substrate material. Unlike previous works on molecular and gas sensing using infrared metasurfaces^[47-50], the working principle of our device does not rely on the analyte molecules being in the near-field of the metasurfaces, e.g. through physical adsorption, making our fabricated metasurfaces reusable. We demonstrate the capabilities of our MIR spectrometer as follows. We subject our microspectrometer to various chemicals at various concentrations and feed its output (i.e. thermal camera image) to an ML algorithm to train it to classify ethanol, isopropanol, acetone, and ethyl lactate. We then test our microspectrometer by subjecting it to these chemicals, and we find that its accuracy is unity. We study the detection limit of the platform by quantifying low concentrations of ethyl lactate diluted in cyclohexane down to 0.1%. Lastly, to demonstrate the versatility of our platform, we show the identification of food and drug samples.

2. Results and Discussion

2.1. Operating principle of FADA microspectrometer

Our microspectrometer consist of a plasmonic filter array chip bonded to a detector array. The latter is a thermal imaging bolometer sensor (80 \times 60-pixels). Our FADA microspectrometer represents the experimental realization of our previous simulation-only study^[51]. The operating principle of our

This article is protected by copyright. All rights reserved.

microspectrometer and the experiments conducted in this study are schematically illustrated as **Figure 1a**. The chemical (liquid) to be identified is injected into a flow cell fitted with two sodium chloride windows. The flow cell is placed between the microspectrometer and the infrared light source, which is a blackbody (Figure 1a). Data analysis is performed as follows. The raw image output from the thermal camera is read. It can be seen from Figure 1a that the raw output image contains twenty spots. These correspond to the ten bandstop (upper part of raw output image of Figure 1a) and ten bandpass (lower part) filters. The raw output image is cropped to extract the pixels corresponding to the filters (7×7 pixels). As we describe further below, each filter on the filter array chip has an extent of $150 \mu\text{m} \times 150 \mu\text{m}$, while the pixel pitch is $200 \mu\text{m}$. The inter-filter regions comprise the unpatterned gold film and are thus opaque. We sample these inter-filter regions to mitigate the effect of readout drift. Twenty regions are sampled, each comprising 3×3 pixels. The signal ($px_{ij}(k)$) that would be recorded by the pixel group corresponding to the k^{th} filter element can be modeled as follows:

$$px_{ij}(k) = \int_{\lambda_1}^{\lambda_2} I_s \cdot T_A \cdot R_p \cdot T_k d\lambda \quad (1)$$

where I_s is the power spectrum of the infrared light source, T_A is the analyte transmission spectrum, R_p is the responsivity of the pixel, and T_k is the transmission spectrum of the k^{th} filter element. The raw readout signals recorded from the filter regions (each 7×7 pixels) and from the inter-filter regions (each 3×3 pixels) are averaged and hereafter denoted as RO_k (for the k^{th} channel) and RO_0 , respectively. The latter is subtracted from the former and hereafter referred to as the calibrated readout RO_k^* . Due to the fact that the signal levels from the bandpass and bandstop filter channels are significant, this calibration is done in a pair-wise fashion, i.e. between the signal from a given bandstop/bandpass channel and the averaged signal from all eight inter-filter regions of the

bandstop/bandpass group (Figure 1b). Prior to collecting data from a given chemical, we collect a set of reference readings to mitigate against drift in the source spectrum and/or detector responsivity. These readings are performed with acetone or cyclohexane in the liquid cell. As described later, these solvents are used as diluents in our chemical sensing experiments. One may therefore think of the reference readings as the limiting case of an experiment, in which a given chemical (in the dilutant) is progressively reduced in concentration, i.e. the readout signals in the limit that the concentration approaches zero. The data handling process just described is schematically illustrated as Figure 1b, where we show data recorded from pure ethanol sensing experiments. As we describe further below, the normalized readout values are used to train classifiers for chemical identification ML models and/or regression ML models for predicting the concentration of a given liquid. These models are provided with the normalized readout values obtained with an unknown sample, from which chemical identification and/or concentration prediction is performed.

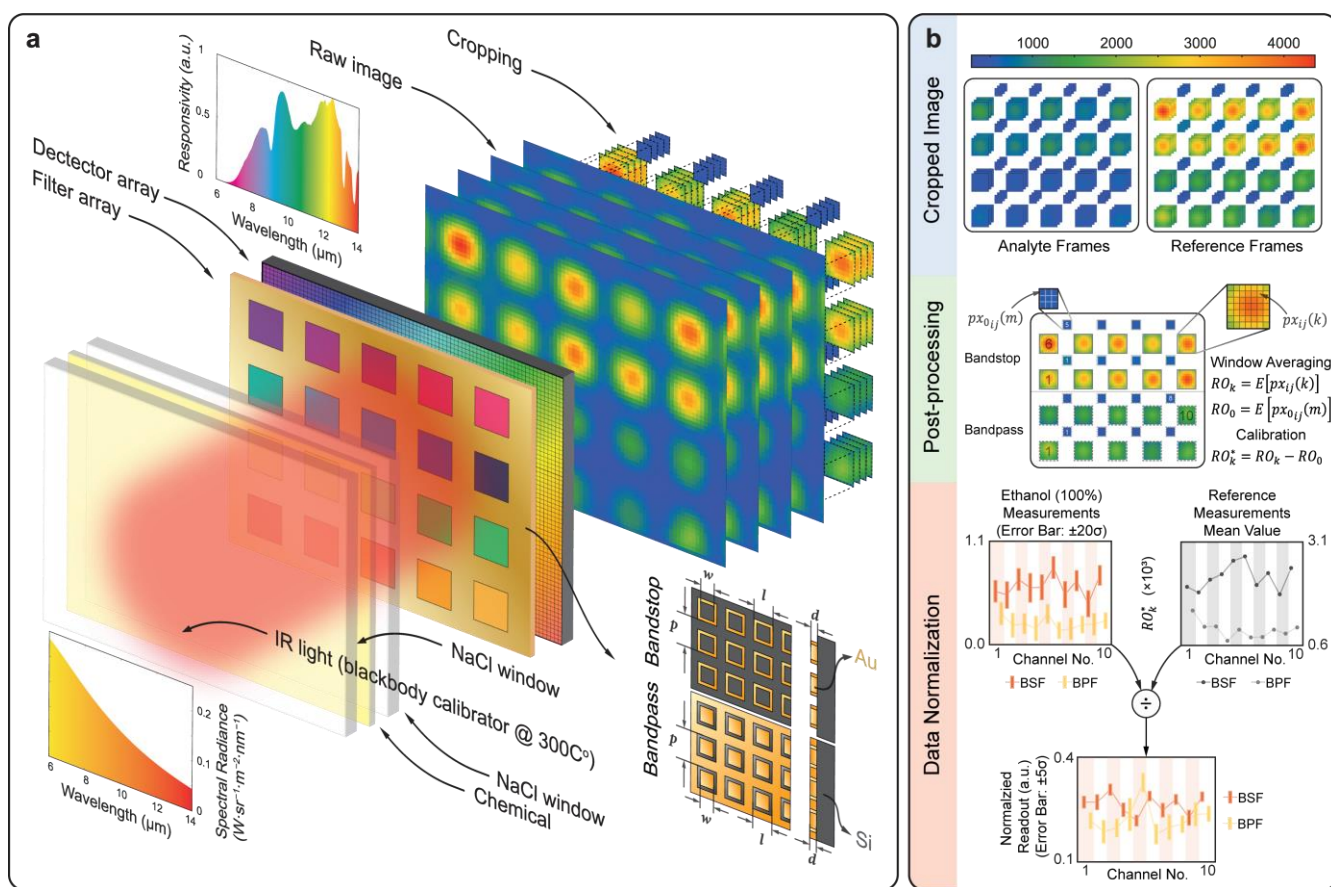


Figure 1. (a) Schematic illustration of the operating principle, data processing and structure of plasmonic filters. Each raw output thermal image can be considered to be the product of source spectrum, material and filter transmission characteristics and thermal camera detector responsivity. Raw images are cropped and post-processed for machine learning (ML) classifier training. (b) Workflow of raw image to normalized readout value conversion, illustrated using data measured for ethanol. Cropped images area first converted to readout values by integrating constituent pixel readings. Readout value for the inter-filter region adjacent to a given filter is subtracted from that filter to mitigate against camera chip drift (offset). Readout out data is normalized using a reference output obtained with only dilutant chemical present in liquid cell.

2.2. FADA spectrometer design and fabrication

We use a thermal imaging camera (FLIR Lepton 2.5) comprising an microbolometer array responsive over a portion of the mid-IR spectrum (wavelength range $\sim 6\text{-}14\ \mu\text{m}$, i.e. approximately $1650\text{-}700\ \text{cm}^{-1}$) that contains numerous molecular vibrational signatures. The small size and low weight furthermore make it ideal for the realization of our FADA microspectrometer. The detector array has 4800 (80×60) pixels with a pitch of $17\ \mu\text{m}$, meaning that the photosensitive region has an extent of $1.36\ \text{mm}\times 1.02\ \text{mm}$. We verify this with a microscope. To maximize the utilization of this region, we design our filter array chip such that it contains 20 filter channels, each having lateral extent $150\ \mu\text{m}\times 150\ \mu\text{m}$, i.e. roughly 9×9 pixels. There is a $50\ \mu\text{m}$ (~ 3 pixel) wide dead space between adjacent filters, included to reduce crosstalk. As noted above, our filter set contains ten bandpass and ten bandstop filters consisting of nano-patterned regions of a gold film ($150\ \text{nm}$ thick) on an undoped silicon wafer. The bandpass filters are arrays of square ring apertures. The bandstop filters are array of square shaped gold rings. This approach was used in our previous simulation-only study^[51], but with aluminum. In this work, we choose a combination of ten bandpass filters and ten bandstop filters. To shift the wavelength of the passband and stopbands to cover the wavelength range $6\text{-}14\ \mu\text{m}$, the geometric parameters (period p , outer length l , and inner length w) are scaled (Table 1). The thickness of the gold film is maintained to minimize fabrication complexity. Further information on the filter optical properties is provided as Supporting Information.

Table 1. Filter Geometric Parameters

	p [μm]	Δp [nm]	l	w	d [nm]
Bandpass	1.9-3.7	200	$0.6p$	$0.4p$	150
Bandstop	1.8-3.6	200	$0.5p$	$0.4p$	150

This article is protected by copyright. All rights reserved.

The fabrication flow is illustrated as **Figure 2a**. We first use electron beam lithography (EBL) to pattern a resist-coated undoped silicon substrate. Gold is then evaporated to a thickness of 150 nm and lift-off is performed. After sample cleaning, the wafer is cut with a wafer saw so that the resultant chip matches the size of the top silicon cap of the thermal camera. We next add the filter chip to the camera using the following steps (Figure 2b). First, the camera is disassembled, i.e. the flat field correction (FFC) and lens modules are detached from the main chassis. Second, we cut the chassis into two halves with a razor blade to expose the top silicon cap. Third, the filter chip is bonded to the silicon cap using a small drop of polymethylmethacrylate (PMMA) resist as adhesive. This step is performed in a flip chip bonder to allow the chip to be aligned to the camera. Note that in this step, the plasmonic layer faces downwards, i.e. it is in contact with the top silicon cap. To complete the integration, we glue the top chassis onto the bottom chassis, repair damaged electrodes and reattach the FFC module. Prior to the integration, we measure the transmission spectra of the fabricated plasmonic filters using an FTIR microscope (Figure 2c). It can be seen that the dips and peaks in the spectra shift to longer wavelength as the periodicity increases. Figure 2d shows scanning electron micrographs (SEM) of the fabricated filter array. These are colored for visualization purposes. Two insets (left side of Figure 2d) are zoomed-in views of the bandstop (top) and bandpass (bottom) filters with the largest period. Filter numbers are listed on the top left corner of each filter element in the array as shown in Figure 2d. Color photographs of the fabricated filter chip after dicing and of the device after the chip bonding are shown in Figure 2e. More details on the device fabrication and characterization can be found in Supporting Information.

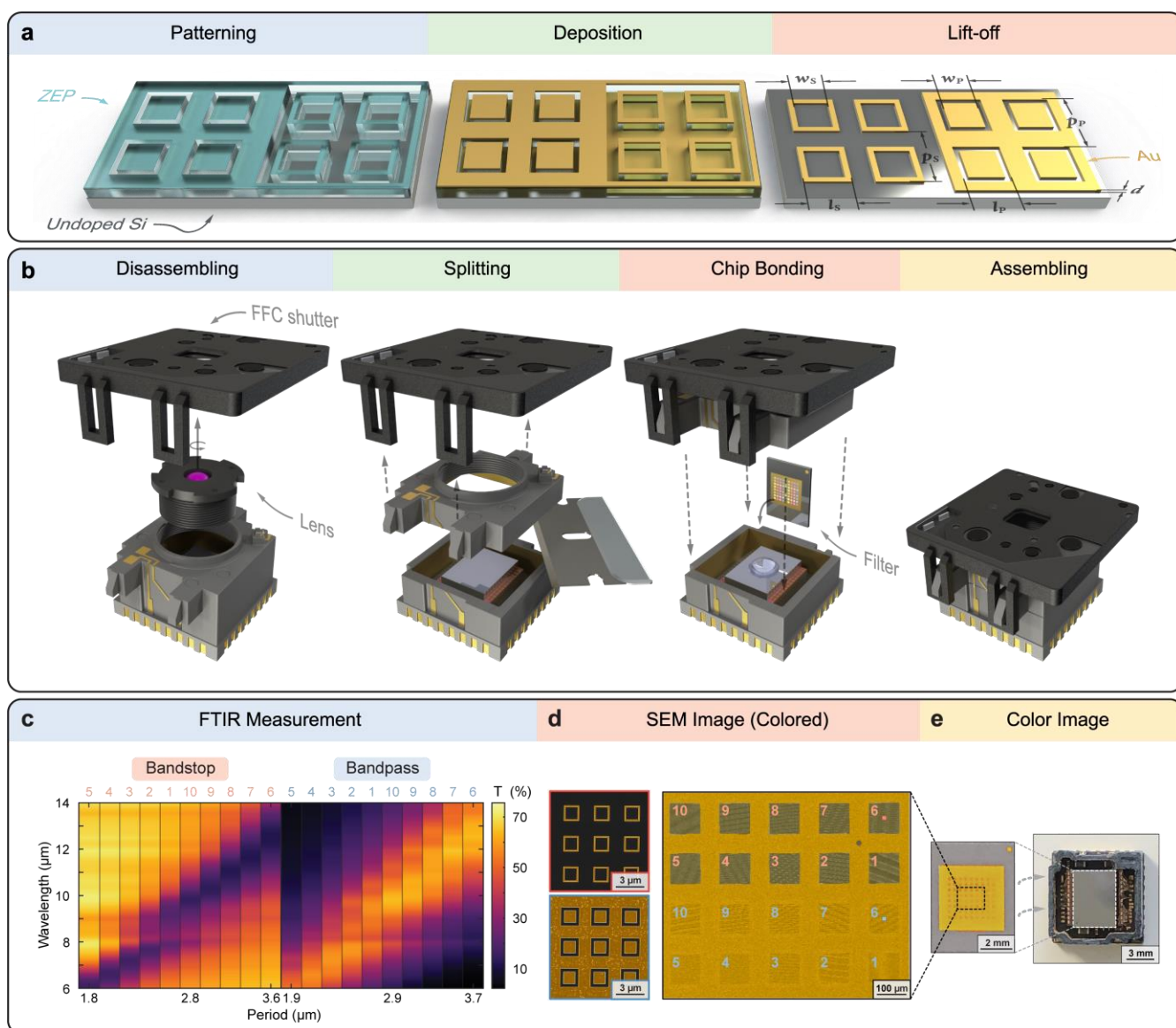


Figure 2. (a) Fabrication of plasmonic filter chip. (b) Steps in integration of filter chip with FLIR lepton camera module. (c) Transmittance spectra of fabricated plasmonic filters measured using FTIR. Bandstop and bandpass filters have transmittance dips and peaks, respectively, spanning the 6-14 μm wavelength range. Filter numbering system used throughout remainder of this paper are as indicated at the top of each plot (5,4,3, etc.). (d) Left: SEM images of selected bandstop (top, channel no. 6) and bandpass (bottom, channel no. 6) filters. Right: SEM images of fabricated filter array, false-colored (e) Color image of the filter array.

This article is protected by copyright. All rights reserved.

for visualization. Filter numbers are shown in top left corners. (e) Photographs of fabricated filter chip and of completed MIR plasmonic microspectrometer.

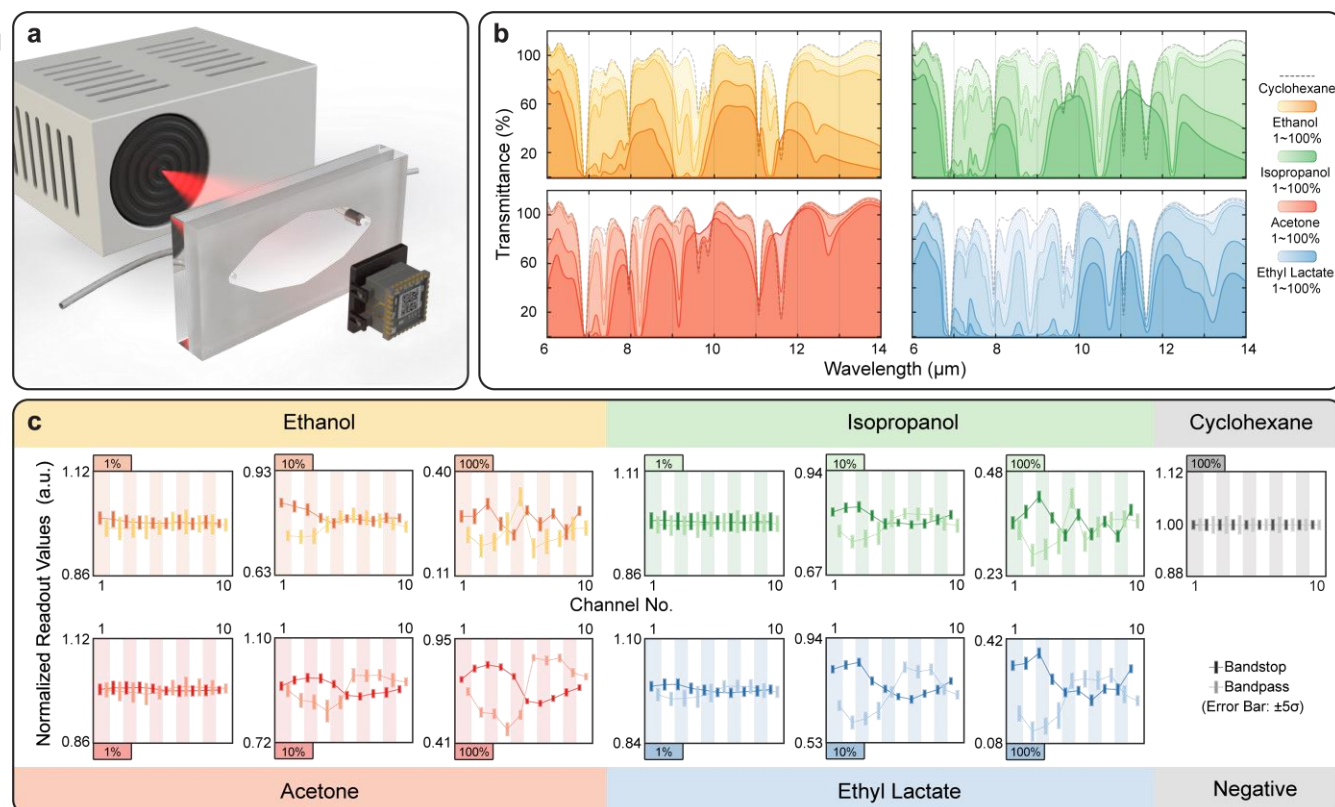


Figure 3. (a) Schematic of experiment setup which consists of a blackbody calibrator as the mid-IR light source, a liquid cell and the microspectrometer. (b) Measured transmittance spectra of selected liquid chemicals diluted in cyclohexane at concentrations of {0, 1, 5, 10, 50, 100%}. (c) Readout data (after post-processing) for four liquid chemicals (ethanol, isopropanol, acetone, ethyl lactate) at three concentrations {1, 10, 100%}. The dilutant cyclohexane serves as the reference. Error bars show five times the standard deviation of the normalized readout values.

2.3. Chemical classification and concentration detection

The experiment set-up is schematically shown as **Figure 3a**. We use a blackbody calibrator as the mid-IR source. The temperature of the blackbody source is set to be 300 °C. The liquid cell has a path length of 50 μm and is placed in between the microspectrometer and the IR light source (see Supporting Information). We first demonstrate classification of the following liquid chemicals: ethanol (EtOH), isopropanol (IPA), acetone (ACE), and ethyl lactate (ELL). This is done for different concentrations. Cyclohexane (Cy) is chosen as the dilutant chemical due to its relatively low absorption across the 6-14 μm range. Figure 2b shows the measured transmittance spectra of all four liquid chemicals diluted in Cy at several selected concentrations ranging from 1% to 100%. We use the experiment setup to acquire raw images when different solutions are in the liquid cell. The raw images are processed to produce the normalized readouts for ML classification model training. The readout data at selected solution concentrations (1, 10, and 100%) are plotted in Figure 3c. For each solution, 300 frames are captured and processed. The captured raw images have excellent signal to noise ratios and we thus use error bars showing five times the standard deviation, as the errors would not be visible if we were to instead use error bars given by the standard deviation. The mean normalized readout values of Cy are all unity because, as described earlier, it is selected to be the denominator in the normalization calculation. From Figure 3c, it can be seen that the readout patterns for the different chemicals are highly distinctive. It can also be seen that for a given chemical, the pattern changes in magnitude as the concentration is varied. All readouts approach unity at low concentration because the transmission spectra become similar to the unmixed Cy reference. This can also be understood from Figure 3b.

We prepare solution samples at several concentrations for readout data acquisition to train a five-class classification model. These classes consist of EtOH, IPA, ACE, ELL and unmixed Cy which is considered the reference channel and denoted ‘negative (Cy 100%)’. The method of data acquisition is provided in Supporting Information. For each of the non-reference classes (i.e. EtOH, IPA, ACE, ELL), 300 data points at six different concentrations (i.e. 1800 data points per chemical class) are plotted in **Figure 4a**. These chemicals diluted in Cy. After the raw image acquisition, cropping and normalization steps described earlier, we perform principal component analysis (PCA) on the raw data (normalized readout values). The data points are projected into principal component (PC) 1 and PC2 space (Figure 4a-left) and into PC2 and PC3 space (Figure 4a-right). Each colored cluster contains 300 points. These are closely packed, due to the high signal to noise ratio of the raw captured images. The insets show data points from the lowest acquired concentration (of 1%) for each chemical and for the Cy reference. As the concentration varies from high to low, the data points follow trajectories that lead toward the ‘negative (0%)’ class. Due to practical considerations, we only sample the readout values at discrete concentration levels. The aim for our platform, however, is to classify chemicals at any concentrations within this range (of 1-100%). We therefore implement an interpolation process to generate additional data to use in the training of ML classifiers. The raw data points are fit to a multivariate Gaussian model to estimate the mean value and covariance of all readouts. We then use this information to generate interpolated data at intermediate concentrations (see Supporting Information). The efficacy of this process was verified in our previous simulation-only study^[51]. A PCA study is conducted on the interpolated data, with the results shown in Figure 4b. It can be seen that cluster traces form trajectories along which the concentration varies. Note there is a crossover of cluster trajectories for EtOH and IPA in low concentration in the first two PC space. The trajectories can however be distinguished by an additional principal component, i.e. PC3 (Figure 4b-right).

This article is protected by copyright. All rights reserved.

It can be seen from Figure 4a,b that the data points corresponding to the four chemicals occur at distinctly different locations in PC space. This suggests that high accuracy classification should be achievable using ML algorithms such as k-nearest neighbors (KNN)^[52], discriminant analysis^[53] and support-vector machines (SVM)^[54]. In this work, we use quadratic discriminant analysis to train classifiers. We first use individual χ^2 tests to determine the feature importance of all PC components. The ranking score is calculated as $-\log(p)$, where p is the p -value of the hypothesis test result, with higher scores indicating features that are more important. The result of the feature importance ranking is shown as Figure 4c. The high scores of the first seven principal components indicate that they are important for this five-chemical classification problem. In order to reduce the computational complexity and prevent overfitting of the trained classifier, we thus use PC1-7 in the training of the classifier. The 10-fold cross-validation prediction accuracy of the trained classifier is 100%. The accuracy is defined as the quotient of the number of correct classifications to the number of training data sets. We acquired an additional data set as a further check of our approach. In this data set, the chemicals are at concentrations (Figure 4d) that differ from those in our original data set. The validation results are presented as a confusion matrix in Figure 4d. It can be seen that the accuracy is again 100%, verifying the efficacy of the classifier and its ability to detect chemicals at arbitrary concentration within the range of 1-100%.

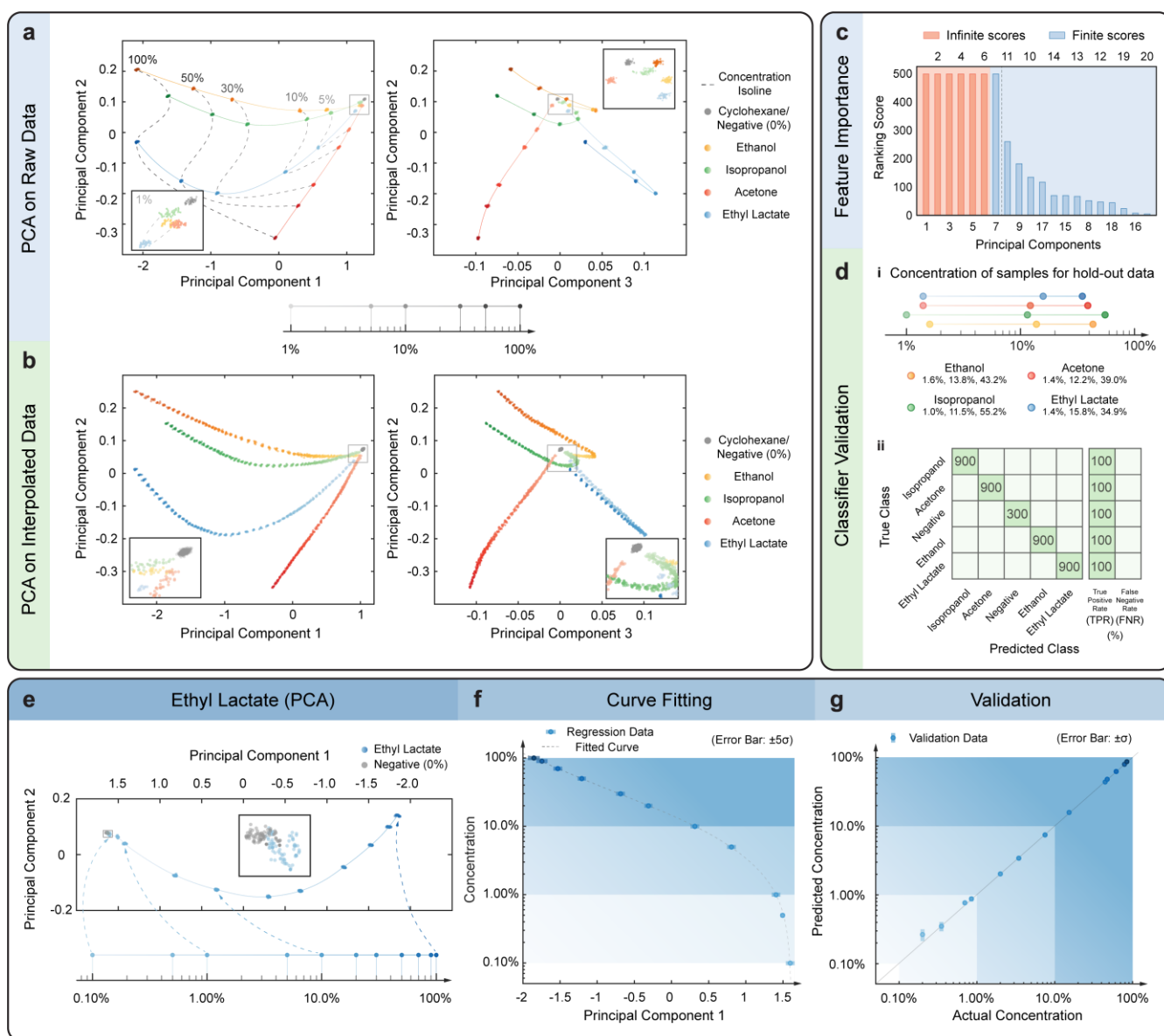


Figure 4. (a) Principal component (PC) analysis of raw data. Plots of data points projected onto (PC1, PC2) space (left) and (PC2, PC3) space (right). Grey dashed lines are the isolines of the concentrations. Insets show the clusters (1% solutions) close to the reference cluster (grey, 0%). Number axis (1-100%, logarithmic scale) shows the concentrations at which the raw data points are acquired. (b) PC analysis of data after interpolation. (c) Feature importance of all 20 filters for four-

This article is protected by copyright. All rights reserved.

chemical classification problem. (d) **(i)** Concentrations at which the hold-out data points are acquired for validation. **(ii)** Hold-out validation result summarized in confusion matrix. (e) PC analysis on ethyl lactate dataset for concentration detection. Acquired concentrations range from 0.1%~100%. (f) Polynomial curve fitting of functional relation between PC1 and concentration. (g) Concentration prediction result using validation data.

We next demonstrate use of the platform to determine the concentration of a known chemical. No changes to the experimental set-up are required. ELL is chosen as the chemical. We acquire new dataset of ELL diluted in Cy at additional concentrations that span the range 0.1% to 100%. The concentrations at which we acquire data are shown in Figure 4e (number axis). We plot the processed data projected to (PC1, PC2) space in Figure 4e. It can be seen that principal component 1 (PC1) and ELL concentration are strongly negatively correlated. We therefore train a non-linear regression model to fit the functional relation between PC1 and ELL concentration. The fitted curve is shown as Figure 4f, with further detail concerning this model provided in Supporting Information. We collected an additional data set as an additional check of our method. A plot of the concentration predicted by our model against the actual concentration is provided as Figure 4g. It can be seen that predicted and actual concentrations are in good agreement, especially at higher concentrations. The root mean square error (RMSE) between predicted and actual concentrations is 0.0104.

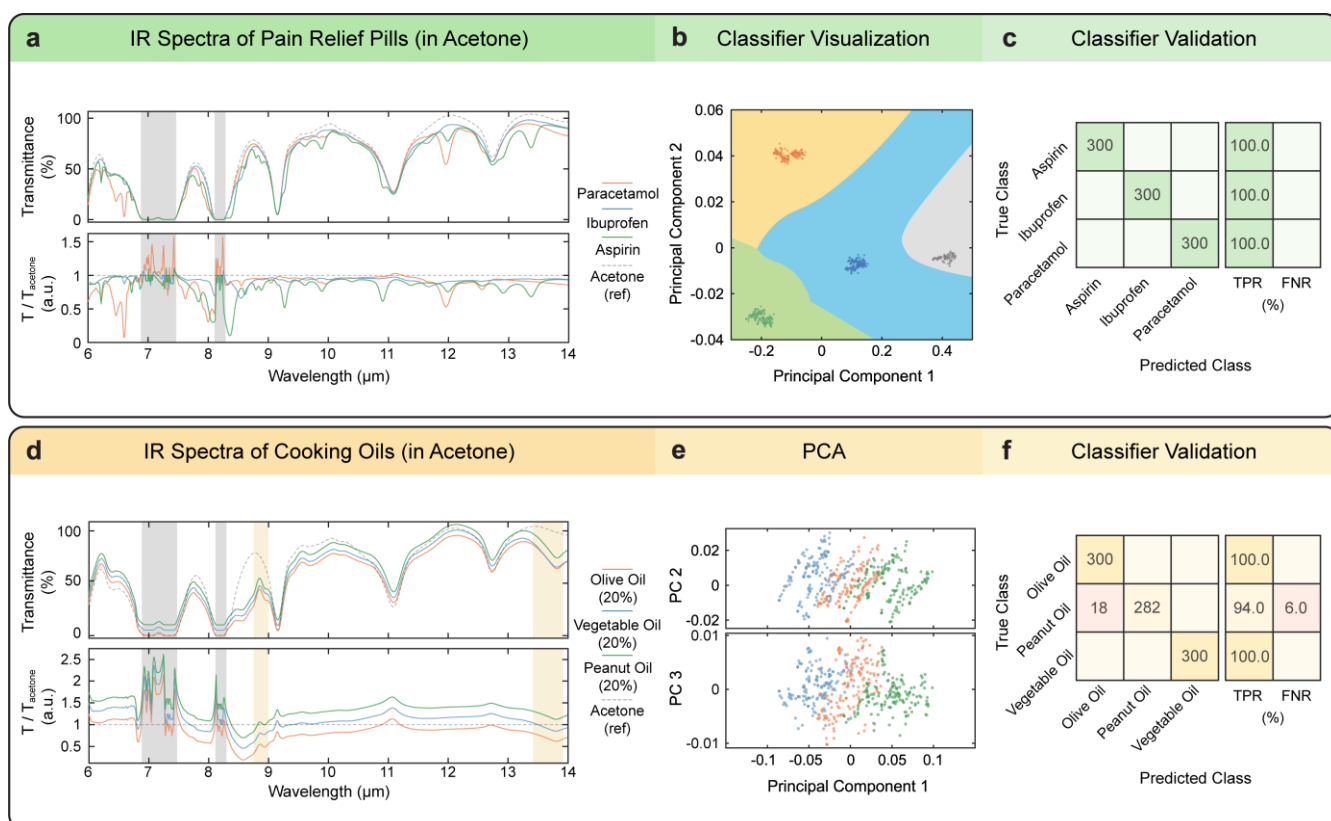


Figure 5. (a) IR spectra of pain relief drugs in acetone solutions. Grey shaded areas denote regions with relative transmittance greater than unity, meaning that the drug-acetone solution has less absorption than pure acetone. (b) Acquired training data points projected onto (PC1, PC2) space. Classifier trained using the first two PCs determines the decision boundaries between drug classes. (c) Drug classification results. (d) IR spectra of common cooking oil in acetone solutions. Note that for better visibility, the spectra of vegetable oil are offset by 5% and 0.25 in the transmittance and normalized transmittance plots, respectively. For peanut oil, offsets of 10% and 0.5 are used. Beige shading indicates regions in which differences between spectra are most perceivable. (e) PCA of cooking oil data showing the first three principal components. (f) Cooking oil classification results.

2.4. Food and drug classification

This article is protected by copyright. All rights reserved.

We next demonstrate the ability of this platform to classify food and drug samples. We first prepare drug solutions. Three kinds of common pain relief pills, including paracetamol (APAP), ibuprofen (IBP) and aspirin (ASP), are ground and mixed with a reference solvent. Here we choose acetone as the reference solvent because the above three drugs have good solubility in acetone. In addition, acetone has lower absorption than other common solvents such as IPA and EtOH (see Figure 3b). We first measure the transmission spectra of drug/acetone solutions using an FTIR spectrometer (**Figure 5a**). We note that in the grey shaded area of the relative transmittance (rT) plot, the rT values are greater than unity, indicating that the drug/acetone mixture has less absorption than neat acetone. We then acquire data with our microspectrometer. We perform PC analysis on the raw data and train a quadratic SVM classifier. When training the classifier, we only use PC1 and PC2 because the data clusters are very well separated. This can be seen from the visualization of datapoints and the classification decision boundaries that are plotted in Figure 5b. We again verify the classifier by hold-out validation. The trained model can correctly classify unseen data with an accuracy of 100% (Figure 5c).

For our food classification experiment, we prepare cooking oil solutions. Three kinds of cooking oil are considered: olive oil (OVO), vegetable oil (VGO) and peanut oil (PNO). Acetone is again used as the dilutant and all solutions are prepared with the same mixing ratio (oil : acetone = 1:4). The purpose of acetone dilution is to reduce the viscosity of sample to maintain a better flow in the liquid cell for repeated measurements. Because all cooking oils share the same main ingredient, i.e. fatty acids, the spectra of the cooking oil samples are very similar, especially when the oils are diluted. The spectra of the oil/acetone samples are plotted in Figure 5d. Note that for visualization purposes, the spectra (transmittance and rT) of VGO are offset by 5% and 0.25 in Figure 5d. Those for PNO are

This article is protected by copyright. All rights reserved.

offset by 10% and 0.5. We use beige shading to indicate the regions with the greatest perceivable differences between spectra. PCA of the data (Figure 5e) shows that the different cluster classes overlap with each other due to the high similarity of their IR fingerprints. We find however that a trained cubic SVM classifier can achieve accuracies between 94 and 100% in a hold-validation test.

3. Conclusion

In this work, we fabricate a filter array detector array (FADA) microspectrometer and implement machine learning (ML) classification algorithms to realize liquid sample identification and concentration detection. We use simulations to design an array of gold plasmonic filters on a silicon substrate. The filter spectral features cover the mid-infrared (mid-IR) wavelength range of 6-14 μm . The fabricated filter array is added to a compact thermal imaging sensor to form the FADA microspectrometer. The raw image output of the sensor is postprocessed into feature vectors for training classification and regression models. The result shows high accuracy in identifying analytes from a group of liquids. We show that the model can also be trained to predict the concentration of a specific liquid sample in a binary mixture with a dilutant down to 0.1%. We furthermore demonstrate food and drug classification using the same system. Numerous applications for infrared spectral analysis exist and many of these would benefit from being implemented using very small, light-weight, low-power and low-cost platforms. Here we have demonstrated such a platform by integrating a plasmonic chip with an uncooled thermal camera. We anticipate many fruitful opportunities for further work, including in both microspectrometer design (e.g. using all dielectric metasurfaces) and in applications (e.g. for the selective and sensitive detection of gases). We also note that the filter integration approach also presents exciting prospects for mid-IR hyperspectral imaging.

Supporting Information

Supporting Information is available from the Wiley Online Library or from the author.

Acknowledgements

This work was supported in part by the Australian Research Council (ARC) Centre of Excellence for Transformative Meta-Optical Systems (Project ID CE200100010) and by the ARC Discovery Projects scheme (DP180104141 and DP210103428). This work was performed in part at the Melbourne Centre for Nanofabrication (MCN) in the Victorian Node of the Australian National Fabrication Facility (ANFF).

Received: ((will be filled in by the editorial staff))

Revised: ((will be filled in by the editorial staff))

Published online: ((will be filled in by the editorial staff))

References

- [1] T. Kwa, R. Wolffenbuttel, *Sensors and Actuators A: Physical* 1992, 31, 259.
- [2] D. S. Goldman, P. White, N. Anheier, *Applied optics* 1990, 29, 4583.
- [3] H. Wu, S. Grabarnik, A. Emadi, G. de Graaf, R. F. Wolffenbuttel, *J. Micromech. Microeng.* 2008, 18.
- [4] J. Correia, G. De Graaf, S. Kong, M. Bartek, R. Wolffenbuttel, *Sens. Actuators, A* 2000, 82, 191.
- [5] J. H. Correia, G. De Graaf, M. Bartek, R. F. Wolffenbuttel, *IEEE Transactions on Instrumentation and Measurement* 2001, 50, 1530.
- [6] N. K. Pervez, W. Cheng, Z. Jia, M. P. Cox, H. M. Edrees, I. Kymissis, *Opt. Express* 2010, 18, 8277.
- [7] A. Emadi, H. Wu, G. de Graaf, R. F. Wolffenbuttel, *Procedia Eng.* 2011, 25, 1401.
- [8] J. Bao, M. G. Bawendi, *Nature* 2015, 523, 67.

This article is protected by copyright. All rights reserved.

- [9] M. Faraji-Dana, E. Arbabi, A. Arbabi, S. M. Kamali, H. Kwon, A. Faraon, *Nat. Commun.* 2018, 9, 4196.
- [10] Z. Wang, S. Yi, A. Chen, M. Zhou, T. S. Luk, A. James, J. Nogan, W. Ross, G. Joe, A. Shahsafi, K. X. Wang, M. A. Kats, Z. Yu, *Nat. Commun.* 2019, 10, 1020.
- [11] J. J. Cadusch, J. Meng, B. Craig, K. B. Crozier, *Optica* 2019, 6, 1171.
- [12] J. Meng, J. J. Cadusch, K. B. Crozier, *Nano Lett.* 2019, 320.
- [13] Z. Yang, T. Albrow-Owen, H. Cui, J. Alexander-Webber, F. Gu, X. Wang, T.-C. Wu, M. Zhuge, C. Williams, P. Wang, A. V. Zayats, W. Cai, L. Dai, S. Hofmann, M. Overend, L. Tong, Q. Yang, Z. Sun, T. Hasan, *Science* 2019, 365, 1017.
- [14] Z. Yang, T. Albrow-Owen, W. Cai, T. Hasan, *Science* 2021, 371.
- [15] B. Redding, S. M. Popoff, H. Cao, *Opt. Express* 2013, 21, 6584.
- [16] B. Redding, S. F. Liew, R. Sarma, H. Cao, *Nat. Photonics* 2013, 7, 746.
- [17] N. Neumann, M. Ebermann, E. Gittler, M. Meinig, S. Kurth, K. Hiller, "Uncooled IR sensors with tunable MEMS Fabry-Pérot filters for the long-wave infrared range", presented at *SENSORS, 2010 IEEE*, 2010.
- [18] C. Gasser, A. Genner, H. Moser, J. Ofner, B. Lendl, *Sens. Actuators, B* 2017, 242, 9.
- [19] A. Fathy, Y. M. Sabry, S. Nazeer, T. Bourouina, D. A. J. M. Khalil, *Nanoengineering*, 2020, 6, 1.
- [20] T. Stark, M. Imboden, S. Kaya, A. Mertiri, J. Chang, S. Erramilli, D. Bishop, *ACS Photonics* 2015, 3, 14.
- [21] M. Nedeljkovic, A. V. Velasco, A. Z. Khokhar, A. Delage, P. Cheben, G. Z. Mashanovich, *IEEE Photonics Technology Letters* 2016, 28, 528.
- [22] M. Muneeb, X. Chen, P. Verheyen, G. Lepage, S. Pathak, E. Ryckeboer, A. Malik, B. Kuyken, M. Nedeljkovic, J. Van Campenhout, G. Z. Mashanovich, G. Roelkens, *Opt Express* 2013, 21, 11659.
- [23] M. A. Druy, A. Emadi, C. D. Brown, H. Wu, G. de Graaf, R. A. Crocombe, R. F. Wolffenbuttel, in *Next-Generation Spectroscopic Technologies III*, 2010, 76800W.
- [24] A. Wang, Y. Dan, *Sci. Rep.* 2018, 8, 1.
- [25] B. Craig, V. R. Shrestha, J. Meng, J. J. Cadusch, K. B. Crozier, *Opt. Lett.* 2018, 43, 4481.
- [26] B. J. Craig, J. Meng, V. R. Shrestha, J. J. Cadusch, K. B. Crozier, *Sci. Rep.* 2019, 9, 13537.

This article is protected by copyright. All rights reserved.

- [27] E. Huang, Q. Ma, Z. Liu, *Sci. Rep.* 2017, 7, 40693.
- [28] Y. Zhu, X. Lei, K. X. Wang, Z. Yu, *Photonics Res.* 2019, 7, 961.
- [29] H. Thienpont, J. Mohr, H. Zappe, H. Nakajima, N. P. Ayerden, M. Ghaderi, M. F. Silva, A. Emadi, P. Enoksson, J. H. Correia, G. de Graaf, R. F. Wolffenbuttel, "Design, fabrication and characterization of LVOF-based IR microspectrometers", presented at *Micro-Optics 2014*, Brussels, Belgium, May 2, 2014, 2014.
- [30] M. Ghaderi, N. P. Ayerden, A. Emadi, P. Enoksson, J. H. Correia, G. de Graaf, R. F. Wolffenbuttel, *J. Micromech. Microeng.* 2014, 24.
- [31] V. Schroeder, E. D. Evans, Y. M. Wu, C. A. Voll, B. R. McDonald, S. Savagatrup, T. M. Swager, *ACS Sens.* 2019, 4, 2101.
- [32] T. Hayasaka, A. Lin, V. C. Copa, L. P. Lopez, R. A. Loberternos, L. I. M. Ballesteros, Y. Kubota, Y. Liu, A. A. Salvador, L. Lin, *Microsyst. Nanoeng.* 2020, 6, 1.
- [33] D. Li, G. Liu, Q. Zhang, M. Qu, Y. Q. Fu, Q. Liu, J. Xie, *Sensors and Actuators B: Chemical* 2021, 331.
- [34] F. S. Fedorov, A. Yaqin, D. V. Krasnikov, V. A. Kondrashov, G. Ovchinnikov, Y. Kostyukevich, S. Osipenko, A. G. Nasibulin, *Food Chem* 2020, 345, 128747.
- [35] C. G. Viejo, S. Fuentes, A. Godbole, B. Widdicombe, R. R. J. S. Unnithan, A. B. Chemical, 2020, 308, 127688.
- [36] FLIR, 2019.
- [37] A. Degiron, H. Lezec, W. Barnes, T. J. A. P. L. Ebbesen, 2002, 81, 4327.
- [38] A. G. Brolo, R. Gordon, B. Leathem, K. L. Kavanagh, *Langmuir* 2004, 20, 4813.
- [39] T. Šíkola, R. D. Kekatpure, E. S. Barnard, J. S. White, P. Van Dorpe, L. Břínek, O. Tomanec, J. Zlámal, D. Y. Lei, Y. Sonnefraud, S. A. Maier, J. Humlíček, M. L. Brongersma, *Appl. Phys. Lett.* 2009, 95.
- [40] Q. Chen, D. R. Cumming, *Opt. Express* 2010, 18, 14056.
- [41] Y. Zhong, S. D. Malagari, T. Hamilton, D. M. Wasserman, *J. Nanophotonics* 2015, 9, 093791.
- [42] Y. Chen, A. Kotnala, L. Yu, J. Zhang, R. Gordon, *Opt. Express* 2015, 23, 30227.
- [43] X. Chong, E. Li, K. Squire, A. X. Wang, *Appl. Phys. Lett.* 2016, 108, 221106.

This article is protected by copyright. All rights reserved.

- [44] A. Braun, S. A. Maier, *ACS Sens.* 2016, 1, 1155.
- [45] Y. D. Shah, J. Grant, D. Hao, M. Kenney, V. Pusino, D. R. S. Cumming, *ACS Photonics* 2017, 5, 663.
- [46] X. He, Y. Liu, K. Ganesan, A. Ahnood, P. Beckett, F. Eftekhari, D. Smith, M. H. Uddin, E. Skafidas, A. Nirmalathas, R. R. Unnithan, *APL Photonics* 2020, 5.
- [47] S. Romano, G. Zito, S. Torino, G. Calafiore, E. Penzo, G. Coppola, S. Cabrini, I. Rendina, V. Mocella, *Photonics Res.* 2018, 6, 726.
- [48] A. Leitis, A. Tittl, M. Liu, B. H. Lee, M. B. Gu, Y. S. Kivshar, H. Altug, *Sci. Adv.* 2019, 5, eaaw2871.
- [49] F. Yesilkoy, E. R. Arvelo, Y. Jahani, M. Liu, A. Tittl, V. Cevher, Y. Kivshar, H. Altug, *Nat. Photonics* 2019, 13, 390.
- [50] X. Xu, H. Li, D. Hasan, R. S. Ruoff, A. X. Wang, D. L. Fan, *Adv. Funct. Mater.* 2013, 23, 4332.
- [51] J. Meng, J. J. Cadusch, K. B. Crozier, *ACS Photonics* 2021, 8, 648.
- [52] N. S. Altman, *Amer. Statist.* 1992, 46, 175.
- [53] R. A. Fisher, *Ann. Eugen.* 1936, 7, 179.
- [54] C. Cortes, V. Vapnik, *Mach. Learn.* 1995, 20, 273.

For Table of Contents Use (Lpor#202100436)

ToC text:

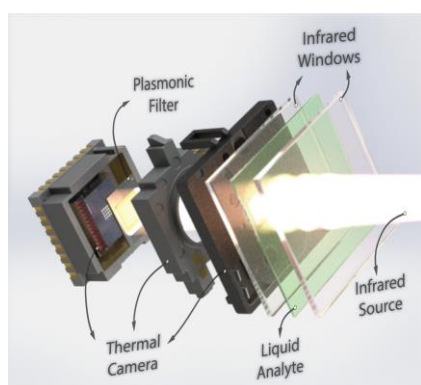
A compact mid-infrared microspectrometer platform for chemical identification has been demonstrated. It consists of a plasmonic metasurface integrated with a thermal camera. Machine learning algorithms are implemented to train classifiers based on data generated by the thermal camera. The high accuracy identification of four liquid

This article is protected by copyright. All rights reserved.

analytes, the concentration quantification of an organic solvent, and the classification of food and drug samples have been demonstrated.

(64 words)

ToC figure (5.5cm*5cm, 600dpi)



This article is protected by copyright. All rights reserved.